
Time-Dependent VAE for Building Latent Factor from Visual Neural Activity with Complex Dynamics

Liwei Huang^{1,2}, ZhengYu Ma², Liutao Yu², Huihui Zhou², Yonghong Tian^{1,2}

¹School of Computer Science, Peking University, China

²Peng Cheng Laboratory, China

Abstract

Seeking high-quality neural latent representations to reveal the intrinsic correlation between neural activity and behavior or sensory stimulation has attracted much interest. Currently, some deep latent variable models rely on behavioral information (e.g., movement direction and position) as an aid to build expressive embeddings while being restricted by fixed time scales. Visual neural activity from passive viewing lacks clearly correlated behavior or task information, and high-dimensional visual stimulation leads to intricate neural dynamics. To cope with such conditions, we propose Time-Dependent SwapVAE, following the approach of separating *content* and *style* spaces in Swap-VAE, on the basis of which we introduce state variables to construct conditional distributions with temporal dependence for the above two spaces. Our model progressively generates latent variables along neural activity sequences, and we apply self-supervised contrastive learning to shape its latent space. In this way, it can effectively analyze complex neural dynamics from sequences of arbitrary length, even without task or behavioral data as auxiliary inputs. We compare TiDe-SwapVAE with alternative models on synthetic data and neural data from mouse visual cortex. The results show that our model not only accurately decodes complex visual stimuli but also extracts explicit temporal neural dynamics, demonstrating that it builds latent representations more relevant to visual stimulation.

1 Introduction

With the rapid development of neural recording technologies, researchers are now able to simultaneously record the spiking activity of large populations of neurons, providing new avenues for exploring the brain [29]. This type of data has sparked strong interest in proposing new methods to uncover the underlying dynamical structure of neural population activity related to brain functions, usually called latent variable methods [31, 30, 23]. These methods aim to capture the variability in simultaneously recorded neural population data with a limited number of latent variables, providing insights into neural representation, and its relationship with cognition or behavior [10, 15, 18]. Popular methods include principal component analysis [28, 3, 6], factor analysis [34, 24, 11, 9], Gaussian process [32, 35], and variational models [13, 22, 36, 19]. Most of these studies have dealt with neural population data recorded from the motor system [34, 6, 22, 36, 19, 25], while only a few have dealt with data from the visual system [11, 25], or other brain areas [28, 3].

Passive viewing of visual stimuli is an important and commonly adopted experimental paradigm, especially for exploring visual coding and processing [27]. Most latent variable models for studying visual neural activity are limited to simple stimuli, e.g., drifting gratings, and encounter some constraints for complex natural stimuli, such as imposing a strong prior assumption about the dynamics of the latent space [11, 13, 35] and processing each time window independently [21]. Recently, to deal with neural activity with complex dynamics under movie stimuli, Schneider et al.

proposed CEBRA, producing consistent and high-performance latent representations using fixed temporal filters [25]. Yet, effectively exploiting the temporal dependence of variable-length sequences to discover latent manifolds, in the absence of task or behavioral information, is still challenging.

To address this problem, we innovatively propose Time-Dependent SwapVAE (TiDe-SwapVAE), which utilizes state variables to construct conditional distributions for *content* and *style* latent variables with temporal dependence. We evaluate our model on synthetic and mouse visual datasets. We show that our model builds meaningful latent representations that are highly correlated with complex visual stimuli, which gives new insights into the intrinsic relationship between neural activity and visual stimulation. Specifically, our main contributions are as follows.

- Based on Swap-VAE [19], we modify the assumption of independence along time and introduce state variables to accumulate and filter temporal information, so that we can construct highly time-dependent latent spaces. Our model is able to progressively compress neural activity along a chronological order in a natural way.
- Through evaluation on mouse visual datasets, we demonstrate that our model efficiently decodes neural activity to related natural scenes or natural movies, showing the highest performance compared to alternative models.
- Through visualization of latent representations, we provide evidence that our model captures explicit temporal structures of neural dynamics for different time scales.

2 Related work

VAE for population neural data analysis As the advancement of deep learning, VAE-based approaches have been proposed to discover latent variables underlying population neural activity, better elucidating the mechanisms of neural representation. Latent factor analysis via dynamical systems (LFADS) used RNNs in a modified sequential VAE framework, accurately predicting observed behavioral variables and extracting precise firing rate estimates on single trials from several motor cortical datasets [22, 16]. pi-VAE, incorporating the relationship between the latent and task variables, constructed interpretable and identifiable latent variables [36]. To learn disentangled latent neural representations without labels, Swap-VAE combined a generative modeling framework with self-supervised learning based on an alignment loss, building latent factors linked to behavior [19]. CEBRA, a self-supervised learning algorithm, obtained consistent embeddings of high-dimensional recordings using auxiliary variables [25].

Visual neural data analysis via latent variables With the growth of simultaneously recorded neural population data from the visual cortex, latent variable methods have been applied to extract underlying manifolds of neural activity. For population activity in macaque V1, some work used GPFA and found that anesthesia-induced network state fluctuations lead to correlated variability [11], while another proposed nonlinear generative fLDS, capturing neural variability with a few latent dimensions under drifting grating stimulus [13]. A rectified latent variable model built latent variables that show a spectrum of functional groups as neurons in the murine visual cortex under drifting gratings [21]. [25] achieved rapid, high-accuracy decoding of natural videos.

3 Time-Dependent SwapVAE

Basic Notations Considering the neural activity of a population of neurons over a period of time, we define a sequence input as $\mathbf{x} = (\mathbf{x}_1, \mathbf{x}_2, \dots, \mathbf{x}_T) \in \mathbb{R}^{T \times N}$, which represents spike counts of N neurons within T small time windows. The output $\mathbf{r} = (\mathbf{r}_1, \dots, \mathbf{r}_T) \in \mathbb{R}^{T \times N}$ is an estimate of firing rates of the input. The low-dimensional latent representation of time point t is denoted as $\mathbf{z}_t \in \mathbb{R}^M$.

3.1 Model Architecture

Our goal is to compress temporal neural activity into high-quality latent spaces with modeling the temporal relationship of sequences. Motivated by these considerations, we explicitly model the time dependence between latent variables across time steps on the basis of Swap-VAE [19]. Specifically, we divide the latent space into content space and style space ($\mathbf{z}_t = [\mathbf{z}_t^{(c)}, \mathbf{z}_t^{(s)}]$), just like Swap-VAE.

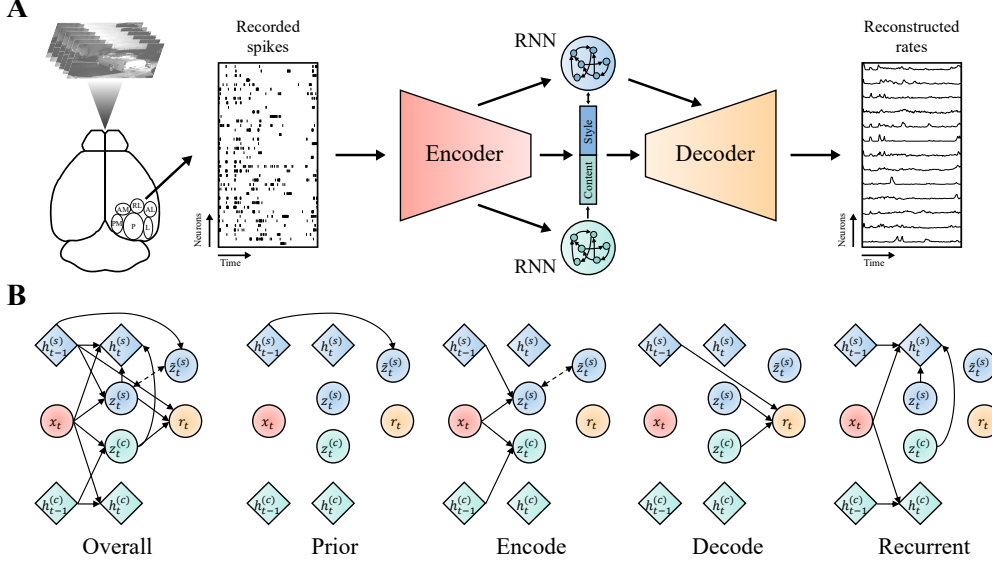


Figure 1: The method overview. **A.** The illustration of TiDe-SwapVAE for analyzing neural activity of the mouse visual cortex during passive viewing. The encoder of our model extracts features from sequential spike data. The latent variables are built conditioned on features from encoder and state variables of RNN to consider temporal dependence. The decoder maps latent variables to reconstructed firing rates. **B.** The illustrations of modules in our model. (see details in Section 3.1)

However, instead of assuming that the latent space is independent along the time dimension, we introduce the state variable \mathbf{h}_t to sift and accumulate temporal information [2, 12, 5], so that the latent and output variables of the current time step are conditioned on the input and state variables of the subsequent time steps. Consequently, we name our model as Time-Dependent SwapVAE. The operation of each module in our model is shown in Figure 1, and we formulate them below.

Encode As we add the state variables, the latent space is constructed not only from \mathbf{x}_t but also from \mathbf{h}_{t-1} . While the content latent variables are constructed as deterministic values, the style latent variables are constructed as a parameterized conditional distribution (approximate posterior):

$$\mathbf{z}_t^{(c)} = f_{\text{enc}}^{(c)} \left(f_{\mathbf{x}}(\mathbf{x}_t), \mathbf{h}_{t-1}^{(c)} \right), \quad (1)$$

$$\mathbf{z}_t^{(s)} \mid \mathbf{x}_{1:t}, \mathbf{h}_{1:t-1}^{(s)} \sim \mathcal{N}(\boldsymbol{\mu}_{z,t}, \boldsymbol{\sigma}_{z,t}^2 \cdot \mathbf{I}), [\boldsymbol{\mu}_{z,t}, \boldsymbol{\sigma}_{z,t}] = f_{\text{enc}}^{(s)} \left(f_{\mathbf{x}}(\mathbf{x}_t), \mathbf{h}_{t-1}^{(s)} \right), \quad (2)$$

where f_x , $f_{\text{enc}}^{(c)}$ and $f_{\text{enc}}^{(s)}$ are all parameter-learnable neural networks for extracting features from the input and computing the latent variables, respectively. The similar functions of f in the following text are also trainable neural networks.

Prior Similar to the variational approximate posterior, the prior of $\mathbf{z}_t^{(s)}$ is conditioned on \mathbf{h}_{t-1} for temporal dependence. The distribution is formulated as:

$$\tilde{\mathbf{z}}_t^{(s)} \mid \mathbf{h}_{1:t-1}^{(s)} \sim \mathcal{N}(\tilde{\boldsymbol{\mu}}_{z,t}, \tilde{\boldsymbol{\sigma}}_{z,t}^2 \cdot \mathbf{I}), [\tilde{\boldsymbol{\mu}}_{z,t}, \tilde{\boldsymbol{\sigma}}_{z,t}] = f_{\text{prior}}^{(s)} \left(\mathbf{h}_{t-1}^{(s)} \right). \quad (3)$$

Decode The decoder aims to reconstruct the neural activity input, which receives the full latent variables and the state variables of the style space. Since the input is a sequence of spike counts, we denote the reconstructed responses as a parameterized Poisson distribution [22, 13], i.e., the actual output of the decoder is spike firing rates:

$$\hat{\mathbf{x}}_t \mid \mathbf{z}_{1:t}^{(c)}, \mathbf{z}_{1:t}^{(s)}, \mathbf{h}_{1:t-1}^{(s)} \sim \text{Poisson}(\mathbf{r}_t), \mathbf{r}_t = f_{\text{dec}} \left(\mathbf{z}_t^{(c)}, \mathbf{z}_t^{(s)}, \mathbf{h}_{t-1}^{(s)} \right). \quad (4)$$

Recurrent The state variable is updated by recurrent neural networks, GRU [4]. Through selective integration and utilization of input and latent variables, the state variable is crucial for learning complex sequential dynamics. The updated functions are as follows:

$$\mathbf{h}_t^{(c)} = f_{\text{GRU}}^{(c)} \left(f_{\mathbf{x}}(\mathbf{x}_t), \mathbf{h}_{t-1}^{(c)} \right), \quad (5)$$

$$\mathbf{h}_t^{(s)} = f_{\text{GRU}}^{(s)} \left(f_{\mathbf{x}}(\mathbf{x}_t), \mathbf{z}_t^{(c)}, \mathbf{z}_t^{(s)}, \mathbf{h}_{t-1}^{(s)} \right). \quad (6)$$

3.2 Model Learning

We use self-supervised contrastive learning to jointly train the parameters of all modules in our model. For a given sample $\mathbf{x} = (\mathbf{x}_1, \dots, \mathbf{x}_T)$, we randomly select another sequence offset by several time steps as a positive sample, denoted $\mathbf{x}_{\text{pos}} = (\mathbf{x}_{1+\Delta}, \dots, \mathbf{x}_{T+\Delta})$, where Δ can be positive or negative. In this work, the offset is always less than the length of the sequence, ensuring that the positive sample pairs have overlaps. After building positive pairs, we follow the design of Swap-VAE. On the one hand, we are encouraged to bring the content latent variables of the positive pairs closer together. On the other hand, we swap the content latent variables between the positive pairs while maintaining the style space to construct swapped latent representations and use them to compute new reconstructed firing rates $\hat{\mathbf{r}}$ and $\hat{\mathbf{r}}_{\text{pos}}$.

As we introduce time dependence into our model, we extend the evidence lower bound of VAE to a time-wise version and add the objective function for contrastive learning, which together form the loss function of TiDe-SwapVAE:

$$\mathcal{L} = \mathcal{L}_{\text{recons}} + \mathcal{L}_{\text{swap}} + \beta \mathcal{L}_{\text{regular}} + \gamma \mathcal{L}_{\text{contrast}}, \quad (7)$$

where β and γ are hyperparameters that serve to control the severity of penalty for each loss terms. The reconstruction loss $\mathcal{L}_{\text{recons}}$ and the swapped reconstruction loss $\mathcal{L}_{\text{swap}}$ is time-wise, formulated as $\frac{1}{T} \sum_{t=1}^T [\mathcal{L}_P(\mathbf{x}_t, \mathbf{r}_t) + \mathcal{L}_P(\mathbf{x}_{\text{pos},t}, \mathbf{r}_{\text{pos},t})]$ and $\frac{1}{T} \sum_{t=1}^T [\mathcal{L}_P(\mathbf{x}_t, \hat{\mathbf{r}}_t) + \mathcal{L}_P(\mathbf{x}_{\text{pos},t}, \hat{\mathbf{r}}_{\text{pos},t})]$, respectively. \mathcal{L}_P is Poisson negative log likelihood loss. As for $\mathcal{L}_{\text{contrast}}$, we do not apply time-wise operation, but flatten the temporal and spatial dimensions of the content latent variables from the positive pairs and compute the cosine distance between the two vectors. $\mathcal{L}_{\text{regular}}$ is the KL divergence to measure the difference between the prior and the approximate posterior of the style latent variables, formulated as $\frac{1}{T} \sum_{t=1}^T \left[D_{\text{KL}}(\mathbf{z}_t^{(s)} \parallel \tilde{\mathbf{z}}_t^{(s)}) + D_{\text{KL}}(\mathbf{z}_{\text{pos},t}^{(s)} \parallel \tilde{\mathbf{z}}_{\text{pos},t}^{(s)}) \right]$. As described above, we assume that both distributions are Gaussian, so that the KL divergence can be written explicitly as:

$$D_{\text{KL}}(\mathbf{z}_t^{(s)} \parallel \tilde{\mathbf{z}}_t^{(s)}) = \frac{1}{2} \left(-1 + \frac{(\mu_{z,t} - \tilde{\mu}_{z,t})^2 + \sigma_{z,t}^2}{\tilde{\sigma}_{z,t}^2} - \log \sigma_{z,t}^2 + \log \tilde{\sigma}_{z,t}^2 \right), \quad (8)$$

where all operations are element-wise calculations on vectors.

4 Experiments

4.1 Evaluation and Alternative Models

In this work, we intend to compress neural activity to latent representations that exhibit strong relevance to the visual stimulation. According to this expectation, we evaluate our model from two aspects. First, we quantify the performance on decoding visual stimuli. Second, we assess the clarity of temporal structures extracted from neural dynamics.

For a comprehensive comparative analysis, we compare TiDe-SwapVAE with several latent variable models, including four generative models (an unsupervised: β -VAE [14], a sequential: LFADS [22],

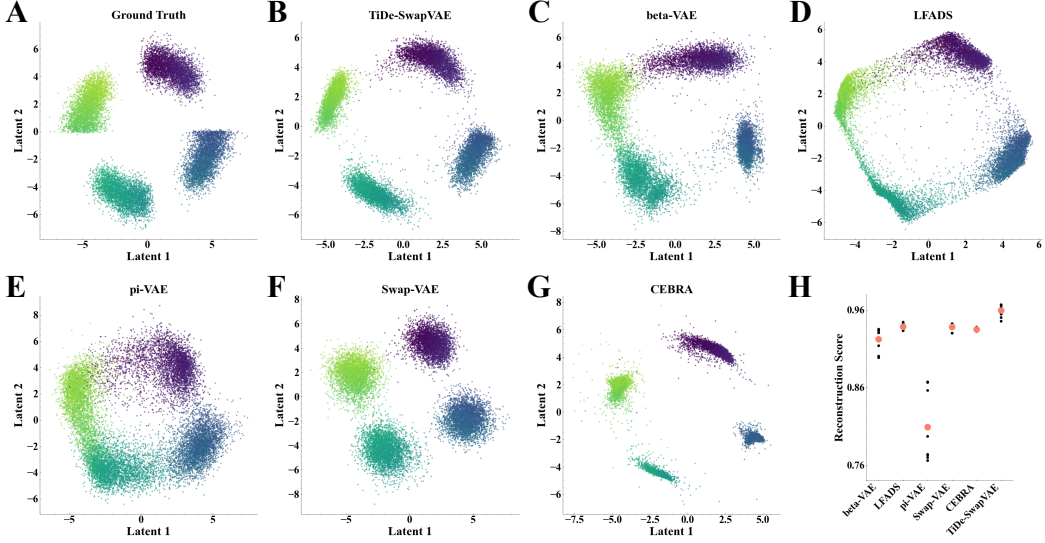


Figure 2: Results of synthetic experiments. **A.** The true latent variables. Different colors correspond to different labels u , gradient from 0 to 2π . **B.** The regressed latent variables of our model. **C-G.** The results of alternative models. **H.** The reconstruction scores of all models. Each black dot represents an individual run, and the red dot represents the average score of ten runs.

a supervised: pi-VAE [36], and a self-supervised: Swap-VAE [19] and a nonlinear encoding method with contrastive learning (CEBRA) [25]. Specifically, β -VAE, pi-VAE and Swap-VAE compress neural activity independently for each time point. LFADS processes sequential neural activity with bidirectional RNNs. CEBRA encodes temporal features of sequence data with fixed convolutional kernels. None of them build the latent representations progressively along the chronological order.

4.2 Experiments on Synthetic Data

We first validate TiDe-SwapVAE on the task of reconstructing the ground truth of synthetic latent variables. The procedure for generating synthetic data follows some previous work [17, 36].

4.2.1 Synthetic Dataset and Experimental Setup

First, we generate labels u_i from four uniform distributions on $[\frac{2i \times \pi}{4}, \frac{(2i+1) \times \pi}{4}]$, $i \in \{0, 1, 2, 3\}$, in preparation for building four clusters. Second, for each cluster, we sample 2-dimensional latent variables \mathbf{z} from independent Gaussian distribution with $(5 \sin u_i, 5 \cos u_i)$ as mean and $(0.6 - 0.5|\cos u_i|, 0.5|\cos u_i|)$ as variance. Third, we feed sampled latent variables into a RealNVP network [8] to form the firing rate of 100-dimensional observations and generate the synthetic neural activity from the Poisson distribution. Each cluster contains 4,000 samples (Figure 2A).

After generation, all samples are split to 80% for training and 20% for test. All models are set up with 32-dimensional latent variables and trained for 1,000 epochs with an optimizer of Adam and a learning rate of 0.0005. We then apply linear regression to map the latent variables of models to the true latent and report R^2 of the linear regression as the reconstruction score. Specially, since the synthetic data does not involve temporal dependence, the length of input sequences is set to 1 even for models that can handle sequential data.

4.2.2 Reconstruction Results

As shown in Figure 2, TiDe-SwapVAE reliably separates the different clusters as well as recovers the structure of true latent variables to form clear arcs. In contrast, some of the alternative models fail to construct similar structures although they separate clusters (Swap-VAE and CEBRA), and others even

Table 1: The decoding scores (%) for natural scenes classification on the mouse visual neural dataset. The standard error is computed for 10 runs with different random initialization.

Models	Mouse 1	Mouse 2	Mouse 3	Mouse 4
PCA (baseline)	20.0	43.2	43.6	20.0
β -VAE	50.0 \pm 2.8	44.8 \pm 1.1	39.2 \pm 2.0	46.0 \pm 3.0
LFADS	43.6 \pm 4.4	48.4 \pm 2.9	48.0 \pm 2.0	47.6 \pm 1.5
pi-VAE	71.6 \pm 3.7	66.0 \pm 2.1	76.0\pm1.5	28.8 \pm 2.8
Swap-VAE	70.4 \pm 3.9	66.0 \pm 1.5	64.0 \pm 2.6	53.2 \pm 2.8
CEBRA	38.8 \pm 1.3	46.8 \pm 2.6	47.2 \pm 2.0	43.2 \pm 2.6
TiDe-SwapVAE	80.8\pm2.1	70.8\pm1.6	63.6 \pm 2.8	56.4\pm2.6

have difficulty distinguishing four clusters (β -VAE, LFADS, and pi-VAE¹). Quantitatively, the results of reconstruction scores also suggest that our model outperforms all alternative models (Figure 2H).

4.3 Experiments on Mouse Visual Cortex Data

We aim to investigate whether TiDe-SwapVAE can build meaningful latent representations to reveal the intrinsic correlation between neural activity and visual stimulation. Therefore, we utilize a subset of the Allen Brain Observatory Visual Coding dataset [27] for evaluation, which has been used in a variety of work, such as constructing brain-like networks [26], modeling functional mechanisms [1, 7], and decoding neural representations [25]. This dataset is collected by Neuropixel probes from 6 mouse visual cortical regions simultaneously, including VISp, VISl, VISrl, VISal, VISpm, and VISam. Notably, the neural activity was recorded while mice were passively viewing visual stimuli (natural scenes and natural movie) without any task-driven behavior.

The dataset contains 32 sessions, each for one mouse. Since the class of neurons responsive to natural scenes or movies is found in six visual regions, in this work we choose to analyze the neural activity of four mice that have as many neurons as possible (about 300, see Appendix C for exact numbers) with them evenly distributed across all regions.

4.3.1 Visual Dataset under Static Natural Scenes Stimuli and Experimental Setup

First, we focus on neural activity in response to natural scenes. There are 118 natural scenes presented in random order, each for 250ms and 50 trials. We select five scenes that elicit the strongest average responses in four mice for experiments. The neural activity in the form of spike counts is binned into 10ms windows so that each trial contains 25 time points. We randomly split each dataset (one mouse) across all trials into 80% for training, 10% for validation, and 10% for test, and ensure that each subset has an equal number of trials per scene.

In this experiment, we set all models to have 128-dimensional latent space and train them for 200 epochs. The optimizer is also set to Adam with a learning rate of 0.0001. At the training stage, for the three models dealing with sequence data (LFADS, CEBRA and TiDe-SwapVAE), each sample is sequential neural activity from 5 time points. For self-supervised learning, the offset of positive samples from target samples is within ± 3 time points. At the inference stage, we consider the temporal dependence and the assumption that the latent variables of TiDe-SwapVAE are generated by an n-order Markov chain. Consequently, for a target time point, we form a sequence data including its antecedent n time points and its own to compute the latent variables (here n=4). For LFADS, we apply the same approach. For CEBRA, following the original approach [25], we take the surrounding points centered on the target point to form a sequence of the same length as during the training stage and compute its latent variables. For other models (β -VAE, pi-VAE and Swap-VAE), each input sample is neural activity of an independent time point, both at the training and inference stages.

To quantify the performance on decoding natural scenes, we first obtain the latent variables of the last 20 time points (50ms-250ms) in each trial, since there is a response latency in the mouse visual cortex for static stimuli [27]. Then, these latent variables are concatenated into a vector as

¹pi-VAE incorporates the label prior during training, but the inferred latent variables are built without the label prior at the evaluation stage. This way is used in all subsequent experiments.

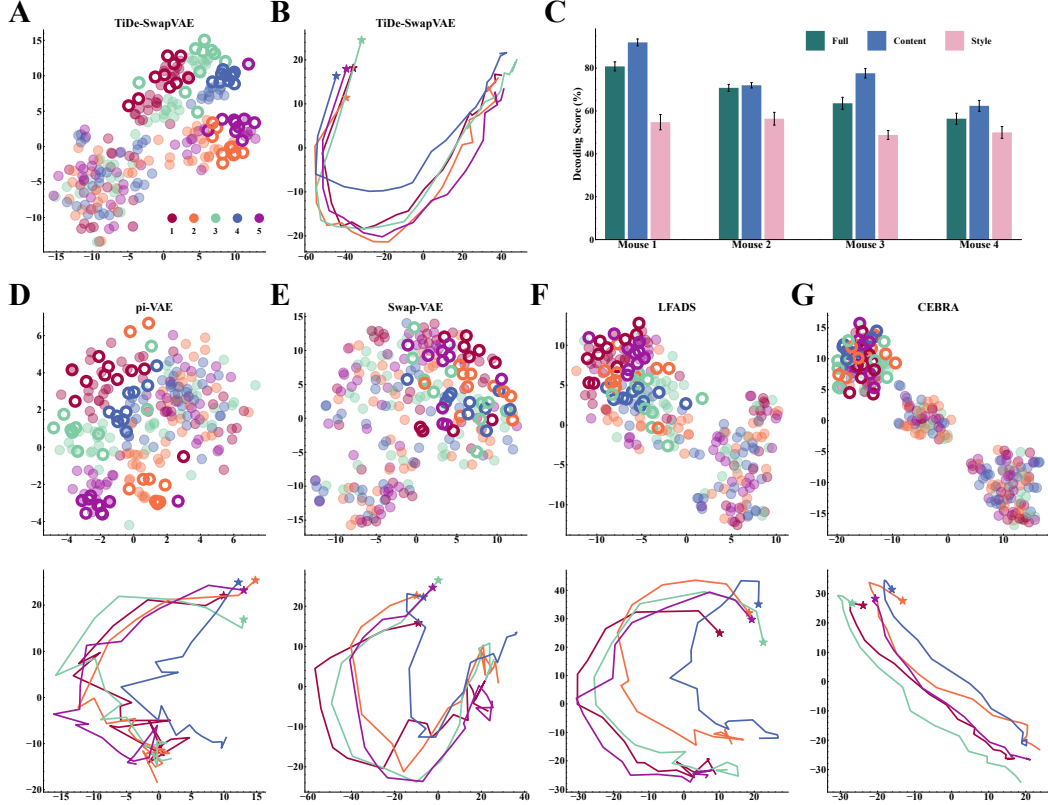


Figure 3: Results on mouse visual cortex dataset under static natural scenes. All dimension reduction is done by tSNE. **A.** The 2-dimensional embedding of the latent representations of our model for each trial. Each color corresponds to a natural scene. Transparent dots denote trials from the training set. Hollow dots denote trials from the test set. **B.** The 2-dimensional embedding of the latent trajectories of our model over time, averaged over all trials for each scene. The asterisk is the starting point. **C.** The decoding scores of the full, content and style latent spaces of our model (mean \pm standard error). **D-G.** The same visualization as **A** and **B** for alternative models.

latent representations of neural activity for that trial. We use the KNN algorithm, a nonparametric supervised learning method, to classify the latent representations of each trial, i.e., to decode the corresponding natural scenes. We search the number of neighbors in odd numbers from 1 to 20 and use the Euclidean distance metric. We fit the KNN using the training set and choose the best number of neighbors on the validation set with classification accuracy as the metric. The accuracy on the test set is reported as the decoding score.

4.3.2 Results of Decoding Natural Scenes and Analysis of Latent Representations

As shown in Table 1, TiDe-SwapVAE achieves the highest decoding scores on three mouse datasets with a noticeable improvement over other models. We observe some meaningful phenomena through comparisons. The fact that pi-VAE introduces class labels of natural scenes in the training stage gives it high decoding scores, but not stably (Mouse 4). The performance of Swap-VAE is consistently good, which suggests that the separation of two types of latent spaces and the swapping operation are indeed effective. However, the other two models (LFADS and CEBRA) that take sequential data as input instead perform poorly on the downstream task, suggesting that their approaches (bidirectional RNNs and temporal filters) of extracting temporal neural features are inappropriate in this case. In contrast, the temporal stepwise computation of our model along the chronological order shows more reliability in exploiting the time dependence. We further evaluate the decoding scores of the content and style latent spaces of our model (Figure 3C) on Mouse 1. We find that the content space yields higher scores than the full space, while the style space shows poor discrimination. The results provide valid evidence for the disentanglement of two spaces of our model.

In addition to the quantitative analysis, we visualize the latent representations by embedding them in two dimensions using tSNE (Figure 3, we focus on Mouse 1 which yields the highest decoding scores. Results of the other three mice are shown in Appendix D). On the one hand, we apply dimension reduction to the representations of each trial (including all time points from 50ms to 250ms), to show the trial-to-trial performance on decoding natural scenes. On the other hand, we reduce the dimensions of a single time point and take the average across trials, to show the latent trajectories over time. For the results of TiDe-SwapVAE, we first observe that most trials are well separated for different classes, especially those from the test set. The latent trajectories capture a similar clear temporal structure with weak class information. For pi-VAE and Swap-VAE, while they are able to discriminate scene classes of the trials, the latter part of latent trajectories show varying degrees of entanglement. As for LFADS and CEBRA, their ability to encode temporal features of sequential neural activity results in explicit temporal evolution, but the latent representations of different classes are largely intermingled. These results suggest that our model effectively distinguishes between category information as well as explicitly captures temporal information from neural dynamics.

This experiment demonstrates the advantages of our model in decoding static natural scene stimuli and extracting fine neural dynamics. However, we also see that the decoding performance for different mice exhibits large differences and the latent representations of some trials are not able to unravel the category entanglement. This may be due to the fact that in the case of passive viewing, the neural activity of different mice and even of different trials from the same individual show huge variability.

4.3.3 Visual Dataset under Natural Movie Stimuli and Experimental Setup

We use neural activity in response to 30s movie stimuli to build the dataset. There are 10 trials and the frame rate of the movie is 30Hz. We bin the spike counts with a sampling frequency of 120Hz and align them with the movie timestamps, resulting in 4 time points for each frame. Similar to the neural dataset under natural scenes, we split the dataset into training, validation and test set.

In this experiment, all models are set up with 128-dimensional latent variables. The number of epochs, the optimizer and the learning rate are the same as for the dataset under natural scenes. For our model, at the training stage, we use neural activity from 4 time points as one sample (also for LFADS and CEBRA) and set the maximum absolute offset to 2. At the inference stage, following the approach in Section 4.3.1, the latent variables of a target time point are generated based on antecedent n time points ($n=3$) and its own. The preprocessing of input samples for the other models is also consistent with Section 4.3.1.

To quantify the performance on decoding natural movie frames, we compute the latent variables of 4 time points within each frame and take the average as latent representations for that frame. KNN is applied to predict the movie frames corresponding to the latent representations (900 frames in total, i.e., 900 classes). Following [25], we take the accuracy measured by considering the error between a predicted frame and the true frame within 1s (default) as a correct prediction. We similarly use the validation set to find the best number of neighbors and report the accuracy of the test set as the decoding score.

4.3.4 Results of Decoding Natural Movie and Analysis of Latent Representations

We find that TiDe-SwapVAE again performs better than alternative models on all four mouse datasets (Table 2). Especially, our model achieves significantly higher decoding scores than LFADS, which is also a sequential VAE. Furthermore, we analyze the decoding scores under different sizes of time window constraints (maximum difference between predicted and real frames) on Mouse 2. The results of Figure 4D show that our model consistently outperforms CEBRA and Swap-VAE across a broad range of window sizes, while CEBRA’s performance degrades faster at smaller size constraints.

We similarly reduce the dimensions of the latent representations of each movie frame for visualization. We set all frames within 1s as a group and show the trajectories of latent representations evolving over time for the middle 10s of the movie (Figure 4A-C, see Appendix D for the results of other parts of the movie). All models present well temporal structure along movie frames. Compared to the two other models, the representations of TiDe-SwapVAE show less overlap and entanglement between different groups.

Our model constructs meaningful latent representations related to the content and temporal structure of movie stimuli at large time scales. At small time scales, although a drop in decoding performance

Table 2: The decoding scores (% in 1s window) for natural movie frame classification on the mouse neural dataset. The standard error is computed for 10 runs with different random initialization.

Models	Mouse 1	Mouse 2	Mouse 3	Mouse 4
PCA (baseline)	8.44	28.77	21.56	11.69
β -VAE	7.32 \pm 0.27	14.93 \pm 0.34	17.56 \pm 0.62	9.44 \pm 0.19
LFADS	9.29 \pm 0.32	26.36 \pm 2.18	25.07 \pm 1.58	11.92 \pm 1.10
pi-VAE	10.19 \pm 0.27	44.83 \pm 0.71	35.84 \pm 0.45	20.22 \pm 0.34
Swap-VAE	10.88 \pm 0.27	43.71 \pm 1.05	35.36 \pm 0.73	19.24 \pm 0.47
CEBRA	9.91 \pm 0.36	44.62 \pm 1.00	39.48 \pm 0.40	21.41 \pm 0.38
TiDe-SwapVAE	12.07\pm0.38	49.01\pm1.10	45.21\pm0.41	21.52\pm0.47

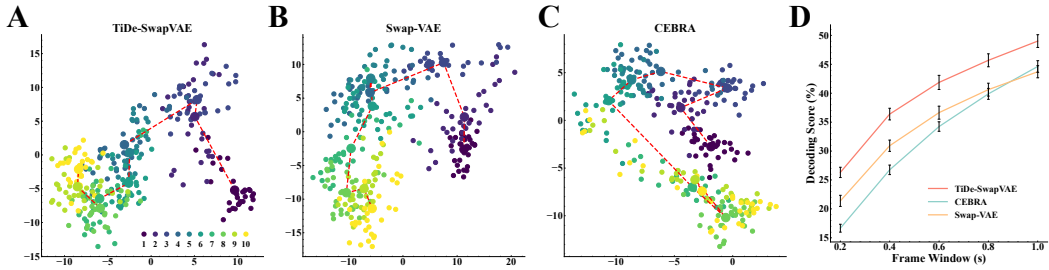


Figure 4: Results on mouse visual cortex dataset under natural movie. All dimension reduction is done by tSNE. **A-C**. The 2-dimensional embedding of the latent representations of our model for each frame. Each color corresponds to all frames within 1s. Each small dots denote one frame. Large dots denote the average among all frames in 1s. The red dashed line connects all averages. **D**. The decoding scores (%) for natural movie frame classification across different time window constraints. Error bars indicate the standard error for 10 runs.

occurs, our model is still better than alternatives. Similar features of adjacent frames may be a factor that makes the latter problem challenging, which may require further exploration.

5 Discussion

This work presents a novel sequential VAE by introducing temporal dependence into a self-supervised generative model, aiming to reveal intrinsic correlations between neural activity from the visual cortex and visual stimulation during passive viewing. Our model, TiDe-SwapVAE, builds latent spaces conditioned on antecedent information to extract low-dimensional time-dependent representations from neural activity. Experiments on synthetic and mouse datasets demonstrate that our model constructs latent representations strongly correlated with the visual stimulation, in terms of decoding natural scenes or movie frames and extracting explicit temporal structure of neural dynamics.

Most latent variable models have focused on neural activity with task-driven behaviors. There is a paucity of research explaining the relationship between neural activity and visual stimuli with this type of model. [25] has made meaningful explorations of the response of the mouse visual cortex with CEBRA. Our work provides more comprehensive experiments of such data, illustrating the validity of latent variable models with temporal dependence for this area of research. However, neural responses elicited by complex natural visual stimuli show large variability across different subjects and different trials [33, 20]. Due to this, our model struggles to maintain stable performance to some extent. Improvements in model structures and learning algorithms are needed to mitigate this limitation.

Last but not least, our approach is not limited to mouse visual neural data and can be extended to neural data of other species or other modalities. As a promising computational model for neuroscience, it may also provide some insights to the field of machine learning.

References

- [1] Shahab Bakhtiari, Patrick Mineault, Timothy Lillicrap, Christopher Pack, and Blake Richards. The functional specialization of visual cortex emerges from training parallel pathways with self-supervised predictive learning. In *Advances in Neural Information Processing Systems 34*, pages 25164–25178, 2021.
- [2] Justin Bayer and Christian Osendorfer. Learning stochastic recurrent networks. *arXiv:1411.7610*, 2014.
- [3] Kevin L Briggman, Henry DI Abarbanel, and WB Kristan Jr. Optical imaging of neuronal populations during decision-making. *Science*, 307(5711):896–901, 2005.
- [4] Junyoung Chung, Caglar Gulcehre, KyungHyun Cho, and Yoshua Bengio. Empirical evaluation of gated recurrent neural networks on sequence modeling. *arXiv:1412.3555*, 2014.
- [5] Junyoung Chung, Kyle Kastner, Laurent Dinh, Kratarth Goel, Aaron C Courville, and Yoshua Bengio. A recurrent latent variable model for sequential data. *Advances in neural information processing systems 28*, pages 2980–2988, 2015.
- [6] Mark M Churchland, John P Cunningham, Matthew T Kaufman, Justin D Foster, Paul Nuyujukian, Stephen I Ryu, and Krishna V Shenoy. Neural population dynamics during reaching. *Nature*, 487(7405):51–56, 2012.
- [7] Saskia EJ de Vries, Jerome A Lecoq, Michael A Buice, Peter A Groblewski, Gabriel K Ocker, Michael Oliver, David Feng, Nicholas Cain, Peter Ledochowitsch, Daniel Millman, et al. A large-scale standardized physiological survey reveals functional organization of the mouse visual cortex. *Nature neuroscience*, 23(1):138–151, 2020.
- [8] Laurent Dinh, Jascha Sohl-Dickstein, and Samy Bengio. Density estimation using real nvp. In *The 5th International Conference on Learning Representations*, 2017.
- [9] Lea Duncker and Maneesh Sahani. Temporal alignment and latent gaussian process factor inference in population spike trains. In *Advances in Neural Information Processing Systems 31*, pages 10466–10476, 2018.
- [10] Lea Duncker and Maneesh Sahani. Dynamics on the manifold: Identifying computational dynamical activity from neural population recordings. *Current opinion in neurobiology*, 70:163–170, 2021.
- [11] Alexander S Ecker, Philipp Berens, R James Cotton, Manivannan Subramaniyan, George H Denfield, Cathryn R Cadwell, Stelios M Smirnakis, Matthias Bethge, and Andreas S Tolias. State dependence of noise correlations in macaque primary visual cortex. *Neuron*, 82(1):235–248, 2014.
- [12] Otto Fabius and Joost R Van Amersfoort. Variational recurrent auto-encoders. *arXiv:1412.6581*, 2014.
- [13] Yuanjun Gao, Evan W Archer, Liam Paninski, and John P Cunningham. Linear dynamical neural population models through nonlinear embeddings. In *Advances in Neural Information Processing Systems 29*, pages 163–171, 2016.
- [14] Irina Higgins, Loic Matthey, Arka Pal, Xavier Glorot, Shakir Mohamed, and Alexander Lerchner. beta-vae: Learning basic visual concepts with a constrained variational framework. In *The 5th International Conference on Learning Representations*, 2017.
- [15] Mehrdad Jazayeri and Srdjan Ostojic. Interpreting neural computations by examining intrinsic and embedding dimensionality of neural activity. *Current opinion in neurobiology*, 70:113–120, 2021.
- [16] Mohammad Reza Keshtkaran and Chethan Pandarinath. Enabling hyperparameter optimization in sequential autoencoders for spiking neural data. In *Advances in Neural Information Processing Systems 32*, pages 15911–15921, 2019.

[17] Ilyes Khemakhem, Diederik Kingma, Ricardo Monti, and Aapo Hyvärinen. Variational auto-encoders and nonlinear ica: A unifying framework. In *The 23rd International Conference on Artificial Intelligence and Statistics*, pages 2207–2217. PMLR, 2020.

[18] Christopher Langdon, Mikhail Genkin, and Tatiana A Engel. A unifying perspective on neural manifolds and circuits for cognition. *Nature Reviews Neuroscience*, 24(6):363–377, 2023.

[19] Ran Liu, Mehdi Azabou, Max Dabagia, Chi-Heng Lin, Mohammad Gheshlaghi Azar, Keith Hengen, Michal Valko, and Eva Dyer. Drop, swap, and generate: A self-supervised approach for generating neural activity. In *Advances in Neural Information Processing Systems 34*, pages 10587–10599, 2021.

[20] Tyler D Marks and Michael J Goard. Stimulus-dependent representational drift in primary visual cortex. *Nature communications*, 12(1):5169, 2021.

[21] Jeremiah B Palmerston and Rosa HM Chan. Latent variable models reconstruct diversity of neuronal response to drifting gratings in murine visual cortex. *IEEE Access*, 9:75741–75750, 2021.

[22] Chethan Pandarinath, Daniel J O’Shea, Jasmine Collins, Rafal Jozefowicz, Sergey D Stavisky, Jonathan C Kao, Eric M Trautmann, Matthew T Kaufman, Stephen I Ryu, Leigh R Hochberg, et al. Inferring single-trial neural population dynamics using sequential auto-encoders. *Nature methods*, 15(10):805–815, 2018.

[23] F Pei, J Ye, D Zoltowski, A Wu, RH Chowdhury, H Sohn, JE O’Doherty, KV Shenoy, MT Kaufman, MM Churchland, et al. Neural latents benchmark’21: Evaluating latent variable models of neural population activity. In *Advances in Neural Information Processing Systems, Track on Datasets and Benchmarks*, 2021.

[24] Patrick T Sadtler, Kristin M Quick, Matthew D Golub, Steven M Chase, Stephen I Ryu, Elizabeth C Tyler-Kabara, Byron M Yu, and Aaron P Batista. Neural constraints on learning. *Nature*, 512(7515):423–426, 2014.

[25] Steffen Schneider, Jin Hwa Lee, and Mackenzie Weygandt Mathis. Learnable latent embeddings for joint behavioural and neural analysis. *Nature*, 617(7960):360–368, 2023.

[26] Jianghong Shi, Bryan Tripp, Eric Shea-Brown, Stefan Mihalas, and Michael A. Buice. Mousenet: A biologically constrained convolutional neural network model for the mouse visual cortex. *PLOS Computational Biology*, 18(9):e1010427, 2022.

[27] Joshua H Siegle, Xiaoxuan Jia, Séverine Durand, Sam Gale, Corbett Bennett, Nile Graddis, Gregory Heller, Tamina K Ramirez, Hannah Choi, Jennifer A Luviano, et al. Survey of spiking in the mouse visual system reveals functional hierarchy. *Nature*, 592(7852):86–92, 2021.

[28] Mark Stopfer, Vivek Jayaraman, and Gilles Laurent. Intensity versus identity coding in an olfactory system. *Neuron*, 39(6):991–1004, 2003.

[29] Anne E Urai, Brent Doiron, Andrew M Leifer, and Anne K Churchland. Large-scale neural recordings call for new insights to link brain and behavior. *Nature neuroscience*, 25(1):11–19, 2022.

[30] Saurabh Vyas, Matthew D Golub, David Sussillo, and Krishna V Shenoy. Computation through neural population dynamics. *Annual review of neuroscience*, 43:249–275, 2020.

[31] Matthew R Whiteway and Daniel A Butts. The quest for interpretable models of neural population activity. *Current opinion in neurobiology*, 58:86–93, 2019.

[32] Anqi Wu, Nicholas A Roy, Stephen Keeley, and Jonathan W Pillow. Gaussian process based nonlinear latent structure discovery in multivariate spike train data. In *Advances in Neural Information Processing Systems 30*, pages 3496–3505, 2017.

[33] Ji Xia, Tyler D Marks, Michael J Goard, and Ralf Wessel. Stable representation of a naturalistic movie emerges from episodic activity with gain variability. *Nature communications*, 12(1):5170, 2021.

- [34] Byron M Yu, John P Cunningham, Gopal Santhanam, Stephen Ryu, Krishna V Shenoy, and Maneesh Sahani. Gaussian-process factor analysis for low-dimensional single-trial analysis of neural population activity. In *Advances in Neural Information Processing Systems 21*, pages 1881–1888, 2008.
- [35] Yuan Zhao and Il Memming Park. Variational latent gaussian process for recovering single-trial dynamics from population spike trains. *Neural computation*, 29(5):1293–1316, 2017.
- [36] Ding Zhou and Xue-Xin Wei. Learning identifiable and interpretable latent models of high-dimensional neural activity using pi-vae. In *Advances in Neural Information Processing Systems 33*, pages 7234–7247, 2020.

A Backbone Structure of TiDe-SwapVAE

The encoder and decoder of our model are kept consistent with Swap-VAE. The encoder consists of three blocks, each of which is sequentially stacked with a linear layer, a batch normalization, and a ReLU activation. The output dimensions of the three linear layers is N , M , and M , where N is the number of neurons and M is the number of latent variables. The decoder is a symmetric structure of the encoder. We set the dimensions of the content and style spaces to be equal. For β -VAE, we use the same backbone structure. For other alternative models, we retain the structure of the original.

In the training, we ensure that the hyperparameters of all models are consistent, obtained by grid search. All models are trained on NVIDIA A100.

B Derivation of the Loss Function of TiDe-SwapVAE

Given that we use state variables and recurrent neural networks to build time dependence in VAE and process sequential data, we need to maximize the likelihood of the joint sequential distribution $p(\mathbf{x}_{1:T})$. Involving the latent variables $\mathbf{z}_{1:T}$, we have the variational lower bound:

$$\begin{aligned}
\log p(\mathbf{x}_{1:T}) &= \int q(\mathbf{z}_{1:T}|\mathbf{x}_{1:T}) \log p(\mathbf{x}_{1:T}) d\mathbf{z}_{1:T} \\
&= \int q(\mathbf{z}_{1:T}|\mathbf{x}_{1:T}) \log \frac{p(\mathbf{x}_{1:T}, \mathbf{z}_{1:T})}{p(\mathbf{z}_{1:T}|\mathbf{x}_{1:T})} d\mathbf{z}_{1:T} \\
&= \int q(\mathbf{z}_{1:T}|\mathbf{x}_{1:T}) \log \frac{q(\mathbf{z}_{1:T}|\mathbf{x}_{1:T})}{p(\mathbf{z}_{1:T}|\mathbf{x}_{1:T})} d\mathbf{z}_{1:T} + \int q(\mathbf{z}_{1:T}|\mathbf{x}_{1:T}) \log \frac{p(\mathbf{x}_{1:T}, \mathbf{z}_{1:T})}{q(\mathbf{z}_{1:T}|\mathbf{x}_{1:T})} d\mathbf{z}_{1:T} \\
&= \text{KL}(q(\mathbf{z}_{1:T}|\mathbf{x}_{1:T})\|p(\mathbf{z}_{1:T}|\mathbf{x}_{1:T})) + \int q(\mathbf{z}_{1:T}|\mathbf{x}_{1:T}) \log \frac{p(\mathbf{x}_{1:T}, \mathbf{z}_{1:T})}{q(\mathbf{z}_{1:T}|\mathbf{x}_{1:T})} d\mathbf{z}_{1:T} \\
&\geq \int q(\mathbf{z}_{1:T}|\mathbf{x}_{1:T}) \log \frac{p(\mathbf{x}_{1:T}, \mathbf{z}_{1:T})}{q(\mathbf{z}_{1:T}|\mathbf{x}_{1:T})} d\mathbf{z}_{1:T},
\end{aligned} \tag{9}$$

where $p(\mathbf{x}_{1:T}, \mathbf{z}_{1:T})$ is the joint distribution as well as $p(\mathbf{z}_{1:T}|\mathbf{x}_{1:T})$ and $q(\mathbf{z}_{1:T}|\mathbf{x}_{1:T})$ is the true posterior and the variational approximate posterior, respectively. The true posterior is intractable.

Considering Eq. 1, Eq. 5 and Eq. 6, we know that $\mathbf{z}_t^{(c)}$ is deterministic values and $\mathbf{h}_t^{(s)}$ is a function of $\mathbf{x}_{1:t}$ and $\mathbf{z}_{1:t}^{(s)}$. Therefore, we have the factorization:

$$p(\mathbf{x}_{1:T}, \mathbf{z}_{1:T}) = \prod_{t=1}^T p(\mathbf{x}_t|\mathbf{z}_{1:t}^{(s)}, \mathbf{z}_{1:t}^{(c)}, \mathbf{x}_{1:t-1}) p(\mathbf{z}_t^{(s)}|\mathbf{x}_{1:t-1}, \mathbf{z}_{1:t-1}^{(s)}), \tag{10}$$

$$q(\mathbf{z}_{1:T}|\mathbf{x}_{1:T}) = \prod_{t=1}^T q(\mathbf{z}_t^{(s)}|\mathbf{x}_{1:t}, \mathbf{z}_{1:t-1}^{(s)}), \tag{11}$$

where $q(\mathbf{z}_t^{(s)}|\mathbf{x}_{1:t}, \mathbf{z}_{1:t-1}^{(s)})$, $p(\mathbf{z}_t^{(s)}|\mathbf{x}_{1:t-1}, \mathbf{z}_{1:t-1}^{(s)})$ and $p(\mathbf{x}_t|\mathbf{z}_{1:t}^{(s)}, \mathbf{z}_{1:t}^{(c)}, \mathbf{x}_{1:t-1})$ are the distributions defined by Eq. 2, Eq. 3 and Eq. 4, respectively. Based on the above factorization, we decompose the variational lower bound as:

$$\begin{aligned}
&\int q(\mathbf{z}_{1:T}|\mathbf{x}_{1:T}) \log \frac{p(\mathbf{x}_{1:T}, \mathbf{z}_{1:T})}{q(\mathbf{z}_{1:T}|\mathbf{x}_{1:T})} d\mathbf{z}_{1:T} \\
&= \int q(\mathbf{z}_{1:T}|\mathbf{x}_{1:T}) \sum_{t=1}^T \left(\log \frac{p(\mathbf{x}_t|\mathbf{z}_{1:t}^{(s)}, \mathbf{z}_{1:t}^{(c)}, \mathbf{x}_{1:t-1}) p(\mathbf{z}_t^{(s)}|\mathbf{x}_{1:t-1}, \mathbf{z}_{1:t-1}^{(s)})}{q(\mathbf{z}_t^{(s)}|\mathbf{x}_{1:t}, \mathbf{z}_{1:t-1}^{(s)})} \right) d\mathbf{z}_{1:T} \\
&= \sum_{t=1}^T \left(\int q(\mathbf{z}_{1:T}|\mathbf{x}_{1:T}) \log \frac{p(\mathbf{x}_t|\mathbf{z}_{1:t}^{(s)}, \mathbf{z}_{1:t}^{(c)}, \mathbf{x}_{1:t-1}) p(\mathbf{z}_t^{(s)}|\mathbf{x}_{1:t-1}, \mathbf{z}_{1:t-1}^{(s)})}{q(\mathbf{z}_t^{(s)}|\mathbf{x}_{1:t}, \mathbf{z}_{1:t-1}^{(s)})} d\mathbf{z}_{1:T} \right).
\end{aligned} \tag{12}$$

When we simplify the above log-likelihood to a function $g(\mathbf{x}_{1:t}, \mathbf{z}_{1:t})$, we have:

$$\begin{aligned}
& \int q(\mathbf{z}_{1:T} | \mathbf{x}_{1:T}) g(\mathbf{x}_{1:t}, \mathbf{z}_{1:t}) d\mathbf{z}_{1:T} \\
&= \int \left(\int q(\mathbf{z}_{1:T-1} | \mathbf{x}_{1:T-1}) q(\mathbf{z}_T^{(s)} | \mathbf{x}_{1:T}, \mathbf{z}_{1:T-1}^{(s)}) g(\mathbf{x}_{1:t}, \mathbf{z}_{1:t}) d\mathbf{z}_T \right) d\mathbf{z}_{1:T-1} \\
&= \int \left(q(\mathbf{z}_{1:T-1} | \mathbf{x}_{1:T-1}) g(\mathbf{x}_{1:t}, \mathbf{z}_{1:t}) \int q(\mathbf{z}_T^{(s)} | \mathbf{x}_{1:T}, \mathbf{z}_{1:T-1}^{(s)}) d\mathbf{z}_T \right) d\mathbf{z}_{1:T-1} \\
&= \int q(\mathbf{z}_{1:T-1} | \mathbf{x}_{1:T-1}) g(\mathbf{x}_{1:t}, \mathbf{z}_{1:t}) d\mathbf{z}_{1:T-1} \\
&= \dots = \int q(\mathbf{z}_{1:t} | \mathbf{x}_{1:t}) g(\mathbf{x}_{1:t}, \mathbf{z}_{1:t}) d\mathbf{z}_{1:t}.
\end{aligned} \tag{13}$$

Therefore, we further decompose Eq. 12 as:

$$\begin{aligned}
& \int q(\mathbf{z}_{1:T} | \mathbf{x}_{1:T}) \log \frac{p(\mathbf{x}_{1:T}, \mathbf{z}_{1:T})}{q(\mathbf{z}_{1:T} | \mathbf{x}_{1:T})} d\mathbf{z}_{1:T} \\
&= \sum_{t=1}^T \left(\int q(\mathbf{z}_{1:t} | \mathbf{x}_{1:t}) \log \frac{p(\mathbf{x}_t | \mathbf{z}_{1:t}^{(s)}, \mathbf{z}_{1:t}^{(c)}, \mathbf{x}_{1:t-1}) p(\mathbf{z}_t^{(s)} | \mathbf{x}_{1:t-1}, \mathbf{z}_{1:t-1}^{(s)})}{q(\mathbf{z}_t^{(s)} | \mathbf{x}_{1:t}, \mathbf{z}_{1:t-1}^{(s)})} d\mathbf{z}_{1:t} \right) \\
&= \sum_{t=1}^T \left(\int q(\mathbf{z}_{1:t} | \mathbf{x}_{1:t}) \log p(\mathbf{x}_t | \mathbf{z}_{1:t}^{(s)}, \mathbf{z}_{1:t}^{(c)}, \mathbf{x}_{1:t-1}) d\mathbf{z}_{1:t} + \right. \\
&\quad \left. \int q(\mathbf{z}_{1:t} | \mathbf{x}_{1:t}) \log \frac{p(\mathbf{z}_t^{(s)} | \mathbf{x}_{1:t-1}, \mathbf{z}_{1:t-1}^{(s)})}{q(\mathbf{z}_t^{(s)} | \mathbf{x}_{1:t}, \mathbf{z}_{1:t-1}^{(s)})} d\mathbf{z}_{1:t} \right) \\
&= \sum_{t=1}^T \left(\int q(\mathbf{z}_{1:t} | \mathbf{x}_{1:t}) \log p(\mathbf{x}_t | \mathbf{z}_{1:t}^{(s)}, \mathbf{z}_{1:t}^{(c)}, \mathbf{x}_{1:t-1}) d\mathbf{z}_{1:t} - \right. \\
&\quad \left. \int q(\mathbf{z}_{1:t-1} | \mathbf{x}_{1:t-1}) \text{KL}(q(\mathbf{z}_t^{(s)} | \mathbf{x}_{1:t}, \mathbf{z}_{1:t-1}^{(s)}) \| p(\mathbf{z}_t^{(s)} | \mathbf{x}_{1:t-1}, \mathbf{z}_{1:t-1}^{(s)})) d\mathbf{z}_{1:t-1} \right) \\
&= \int q(\mathbf{z}_{1:T} | \mathbf{x}_{1:T}) \sum_{t=1}^T \left(\log p(\mathbf{x}_t | \mathbf{z}_{1:t}^{(s)}, \mathbf{z}_{1:t}^{(c)}, \mathbf{x}_{1:t-1}) - \right. \\
&\quad \left. \text{KL}(q(\mathbf{z}_t^{(s)} | \mathbf{x}_{1:t}, \mathbf{z}_{1:t-1}^{(s)}) \| p(\mathbf{z}_t^{(s)} | \mathbf{x}_{1:t-1}, \mathbf{z}_{1:t-1}^{(s)})) \right) d\mathbf{z}_{1:T} \\
&= \mathbb{E}_{q(\mathbf{z}_{1:T} | \mathbf{x}_{1:T})} \left[\sum_{t=1}^T \log p(\mathbf{x}_t | \mathbf{z}_{1:t}^{(s)}, \mathbf{z}_{1:t}^{(c)}, \mathbf{x}_{1:t-1}) - \right. \\
&\quad \left. \text{KL}(q(\mathbf{z}_t^{(s)} | \mathbf{x}_{1:t}, \mathbf{z}_{1:t-1}^{(s)}) \| p(\mathbf{z}_t^{(s)} | \mathbf{x}_{1:t-1}, \mathbf{z}_{1:t-1}^{(s)})) \right].
\end{aligned} \tag{14}$$

Finally, for a given sequential data \mathbf{x} , we have the loss function for training the generative objective:

$$\mathcal{L} \simeq \sum_{t=1}^T \left(\underbrace{-\log p(\mathbf{x}_t | \mathbf{z}_{1:t}^{(s)}, \mathbf{z}_{1:t}^{(c)}, \mathbf{x}_{1:t-1})}_{\text{reconstruction loss}} + \underbrace{\text{KL}(q(\mathbf{z}_t^{(s)} | \mathbf{x}_{1:t}, \mathbf{z}_{1:t-1}^{(s)}) \| p(\mathbf{z}_t^{(s)} | \mathbf{x}_{1:t-1}, \mathbf{z}_{1:t-1}^{(s)}))}_{\text{regularization loss}} \right), \tag{15}$$

where the first and second terms correspond to \mathcal{L}_P and D_{KL} in the main text, respectively.

Since we assume a Poisson distribution for the reconstructed neural activity, \mathcal{L}_P is the Poisson negative log-likelihood:

$$\begin{aligned}
\mathcal{L}_P(\mathbf{x}_t, \mathbf{r}_t) &= -\log \frac{\mathbf{r}_t^{\mathbf{x}_t}}{\mathbf{x}_t!} e^{-\mathbf{r}_t} \\
&= -\mathbf{x}_t \log \mathbf{r}_t + \mathbf{r}_t + \log \mathbf{x}_t! \\
&\approx -\mathbf{x}_t \log \mathbf{r}_t + \mathbf{r}_t + \mathbf{x}_t \log \mathbf{x}_t - \mathbf{x}_t + \frac{1}{2} \log(2\pi\mathbf{x}_t).
\end{aligned} \tag{16}$$

As for D_{KL} , under the assumption that both the prior and the approximate posterior are Gaussian, we have:

$$\begin{aligned}
D_{KL}(\mathbf{z}_t^{(s)} \| \tilde{\mathbf{z}}_t^{(s)}) &= \int q(\mathbf{z}_t^{(s)} | \mathbf{x}_{1:t}, \mathbf{z}_{1:t-1}^{(s)}) \log \frac{q(\mathbf{z}_t^{(s)} | \mathbf{x}_{1:t}, \mathbf{z}_{1:t-1}^{(s)})}{p(\mathbf{z}_t^{(s)} | \mathbf{x}_{1:t-1}, \mathbf{z}_{1:t-1}^{(s)})} d\mathbf{z}_t^{(s)} \\
&= \int q(\mathbf{z}_t^{(s)} | \mathbf{x}_{1:t}, \mathbf{z}_{1:t-1}^{(s)}) \log \frac{\frac{1}{\sqrt{2\pi\sigma_{z,t}^2}} \exp\left(-\frac{(\mathbf{z}_t^{(s)} - \boldsymbol{\mu}_{z,t})^2}{2\sigma_{z,t}^2}\right)}{\frac{1}{\sqrt{2\pi\tilde{\sigma}_{z,t}^2}} \exp\left(-\frac{(\mathbf{z}_t^{(s)} - \tilde{\boldsymbol{\mu}}_{z,t})^2}{2\tilde{\sigma}_{z,t}^2}\right)} d\mathbf{z}_t^{(s)} \\
&= -\frac{\mathbb{E}_{q(\mathbf{z}_t^{(s)})} \left[(\mathbf{z}_t^{(s)} - \boldsymbol{\mu}_{z,t})^2 \right]}{2\sigma_{z,t}^2} + \frac{\mathbb{E}_{q(\mathbf{z}_t^{(s)})} \left[(\mathbf{z}_t^{(s)} - \tilde{\boldsymbol{\mu}}_{z,t})^2 \right]}{2\tilde{\sigma}_{z,t}^2} - \log \sigma_{z,t} + \log \tilde{\sigma}_{z,t} \\
&= -\frac{1}{2} + \frac{\sigma_{z,t}^2 + \boldsymbol{\mu}_{z,t}^2 - 2\boldsymbol{\mu}_{z,t}\tilde{\boldsymbol{\mu}}_{z,t} + \tilde{\boldsymbol{\mu}}_{z,t}^2}{2\tilde{\sigma}_{z,t}^2} - \log \sigma_{z,t} + \log \tilde{\sigma}_{z,t} \\
&= \frac{1}{2} \left(-1 + \frac{(\boldsymbol{\mu}_{z,t} - \tilde{\boldsymbol{\mu}}_{z,t})^2 + \sigma_{z,t}^2}{\tilde{\sigma}_{z,t}^2} - \log \sigma_{z,t}^2 + \log \tilde{\sigma}_{z,t}^2 \right).
\end{aligned} \tag{17}$$

C Characters of the Neural Dataset

In this work, we use a subset of the Allen Brain Observatory Visual Coding dataset [7, 27] recorded from six visual cortical regions of the mouse with Neuropixel probes. The full names and abbreviations of all cortical regions are listed in Table 3. We present the number of neurons for all chosen mouse.

Cortical Region	Abbreviation	Mouse 1	Mouse 2	Mouse 3	Mouse 4
primary visual cortex	VISp	75	51	63	52
lateromedial area	VISl	39	30	38	20
rostrolateral area	VISrl	49	24	44	41
anterolateral area	VISal	42	51	71	46
posteromedial area	VISpm	62	90	19	64
anteromedial area	VISam	94	72	60	64

Table 3: Characters of the neural dataset.

D Additional Visualization of Latent Representations

We visualize the latent representations of TiDe-SwapVAE in experiments of natural scenes for the other three mice and the latent representations of TiDe-SwapVAE, SwapVAE and CEBRA in experiments of natural movie stimuli for other parts of the movie. The results are in line with the conclusion in the main text.

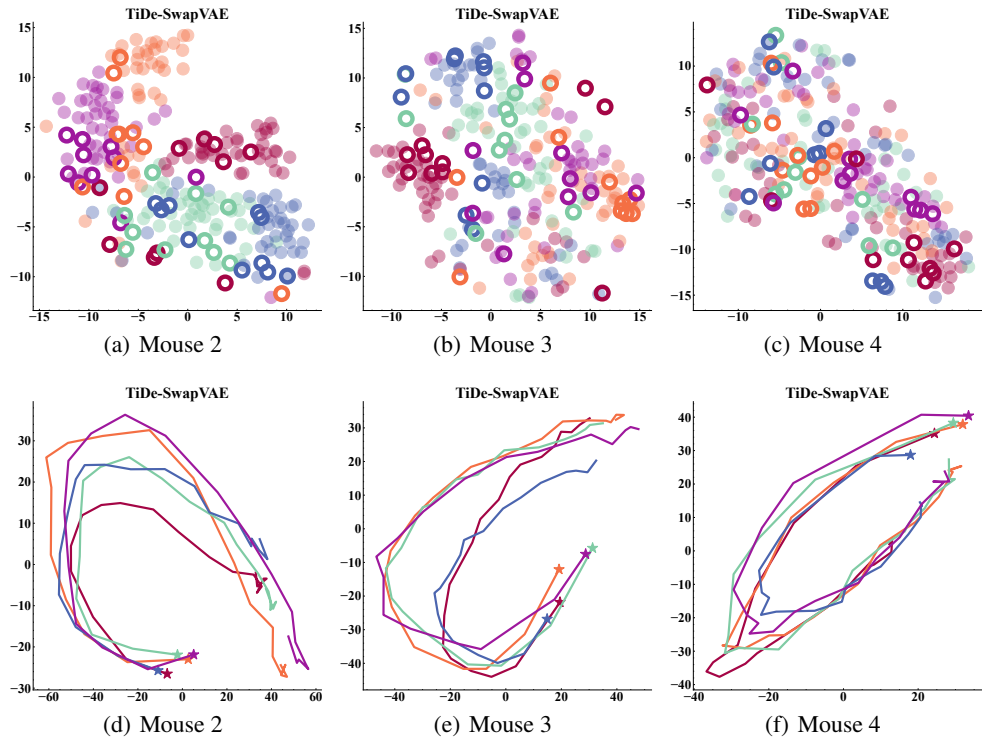


Figure 5: Additional results on mouse visual cortex dataset under static natural scenes.

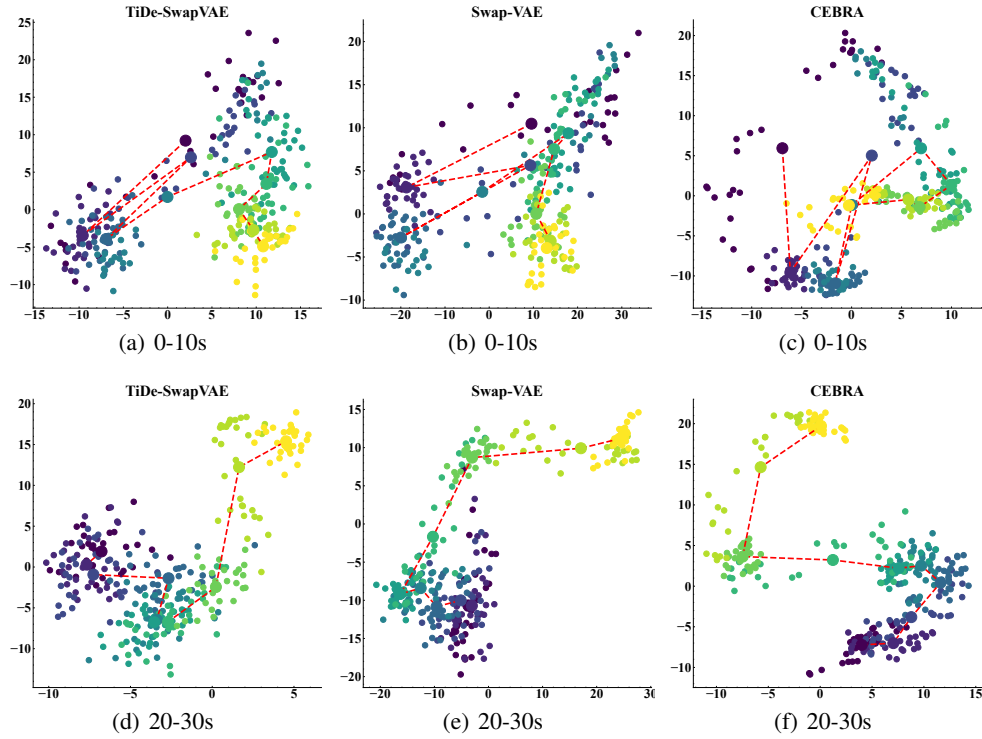


Figure 6: Additional results on mouse visual cortex dataset under natural movie.